ACCSCIENCE PUBLISHING

Asian Journal of Water, Environment and Pollution

ORIGINAL RESEARCH ARTICLE

Unraveling urban greenhouse gas variability in Hefei: Integrating anthropogenic, biogenic, and transport controls on carbon dioxide and methane

Dandan Liu*, Xiangyuan Liu, Ke Tang, and Ping Yu

College of Electrical and Optoelectronic Engineering, West Anhui University, Lu'an, Anhui, China

Abstract

Rapidly industrializing urban regions are critical hotspots for global greenhouse gas (GHG) emissions, yet their specific spatiotemporal dynamics and driving mechanisms remain complex. This study aims to elucidate the long-term variability, co-emission characteristics, and source–sink attributions of atmospheric column-averaged dry-air mole fraction of carbon dioxide (XCO_2) and methane (XCH_4) in Hefei. To achieve this, a comprehensive source–sink–transport framework was employed, integrating long-term satellite retrievals (2009–2020), high-resolution ground-based measurements, atmospheric backward trajectory modeling, and anthropogenic emission inventories. Satellite observations reveal that the XCO_2 growth rate in Hefei (2.41 ± 0.07 ppm/year) exceeded the global average, exhibiting a distinct seasonal maximum in autumn (2.7 ± 0.2 ppm/year). Meanwhile, XCH_4 showed substantial interannual variability that was highly sensitive to regional emission anomalies. Ground-based measurements captured a robust synoptic-scale diurnal co-variation in spring (R^2 = 0.965; $\Delta XCH_4/\Delta XCO_2 \approx 0.007$), indicating dominant fossil fuel co-emissions. Seasonally, strong XCO_2–XCH_4 correlations in spring, autumn, and winter (R^2 > 0.86) confirmed the persistent influence of anthropogenic combustion. However, this correlation significantly weakened in summer (R^2 = 0.66) due to the decoupling effects of biogenic activities and dilution by marine air masses. Supported by backward trajectory and emission inventory analyses, the industrial, construction, and power generation sectors were identified as the primary drivers, contributing over 75% to the regional GHG emission increments. Ultimately, this study highlights the critical role of industrial and power combustion in local atmospheric GHG variability, providing quantitative insights necessary for targeted emission mitigation in super-regional developing hubs.

Keywords: Carbon dioxide; Methane; Hybrid Single Particle Lagrangian Integrated Trajectory model; Seasonal variation; Anthropogenic emission inventory

***Corresponding author:**
Dandan Liu
(baobaoldd@126.com)

Citation: Liu D, Liu X, Tang K, Yu P. Unraveling urban greenhouse gas variability in Hefei: Integrating anthropogenic, biogenic, and transport controls on carbon dioxide and methane. *Asian J Water Environ Pollut.* 2026;23(4):026110070.
doi: 10.36922/AJWEP026110070

Received: March 12, 2026

Revised: April 9, 2026

Accepted: April 9, 2026

Published online: May 18, 2026

1. Introduction

Since the Industrial Revolution, atmospheric greenhouse gas (GHG) concentrations have increased significantly due to human activities.[1,2] Carbon dioxide (CO_2) and methane (CH_4) are critical components of the climate system, playing key roles in determining the Earth's radiative balance.[3,4] While long-term global trends of these gases have been

well recorded,[5-7] spatiotemporal variability at regional and urban scales is poorly constrained because of highly heterogeneous emissions and complex interactions among local sources, atmospheric transport, and biospheric processes.[8,9]

In this regard, rapidly developing urban regions exhibit GHG concentrations that reflect the coupling of surface emissions with meteorological conditions and regional transport, thereby complicating the attribution of local and nonlocal contributions.[10-12] Therefore, observational constraints at these scales are increasingly required to enable a process-level understanding of GHG dynamics and the interpretation of concentration changes in light of their underlying emission mechanisms.[13,14] This remains particularly challenging in economically dynamic areas undergoing rapid urbanization and industrial restructuring.[11]

Hefei is a sub-central city in the Yangtze River Delta, one of China's fastest-growing urban agglomerations in recent decades, with rapid economic growth and extensive urban expansion.[15] Such a development path has structurally increased energy consumption and sustained the rise in anthropogenic GHG emissions.[16,17] However, systematic regional observations and integrated source attribution analyses of atmospheric GHGs remain limited in Hefei. Moreover, multisource datasets—including satellite observations, ground-based measurements, atmospheric transport modeling, and emission inventories—have not been fully integrated into a unified analytical framework, thereby impeding a comprehensive understanding of GHG variability and its driving processes.

Observation of atmospheric column concentrations of GHGs mainly comes from two complementary methods: satellite remote sensing and ground-based measurements. Satellite platforms such as the Greenhouse Gases Observing Satellite (GOSAT) provide extensive spatial coverage and long-term continuity, thus constituting an indispensable source of information on large-scale distribution, seasonal cycles, and interannual variations.[18-20] However, the temporal resolution of satellite retrievals and cloud cover limit their capability to resolve short-term variability.[21,22]

Ground-based Fourier transform spectrometers (FTS), with their high precision and long-term stability, are considered the reference instruments for column observations of GHGs. They are widely used to validate satellite measurements and study local processes.[23,24] The EM27/SUN is portable and, therefore, easily and cost-effectively deployable in urban environments to conduct intensive measurements that capture the short-term variability associated with local emission influences.[25-27]

The concentration of atmospheric GHGs results from both surface emissions and atmospheric transport; therefore, local and regional contributions cannot be easily separated from concentration measurements alone.[28] Backward trajectory models such as the Hybrid Single Particle Lagrangian Integrated Trajectory (HYSPLIT) model are effective tools for diagnosing air-mass origins and transport pathways to assess regional and long-range transport influences on local observations.[29,30] Simultaneously, high-resolution anthropogenic emission inventories are required to describe the sectoral structure of emission sources. The Multi-resolution Emission Inventory for China (MEIC), developed by Tsinghua University, provides gridded emission estimates of CO_2 from major sectors including power generation, industry, residential consumption, and transport, and has thus been a key dataset in atmospheric composition studies over China.[30,31]

However, despite continuous advancements in these individual observational and modeling approaches, significant research gaps persist in the available literature. Most existing studies have relied predominantly on single-platform observations or isolated analytical methods, either focusing solely on large-scale satellite observations or limiting their scope to local ground-based measurements without robust trajectory and inventory constraints.[19-22,25-27]

Consequently, three critical knowledge gaps remain: First, the complex interplay among local anthropogenic emissions, biogenic processes, and regional atmospheric transport remains poorly disentangled, particularly in dynamically evolving urban hubs. Second, the seasonal temporal decoupling of co-emitted species has not been sufficiently quantified at the urban scale. Third, there is an urgent need for an integrated analytical framework that bridges the long-term, large-scale trends captured by satellites with the high-resolution synoptic dynamics observed by ground-based instruments. These limitations significantly impede a comprehensive, process-level understanding of regional GHG dynamics.

Within this context, the present study focuses on the Hefei region by developing a combined analytical framework, including GOSAT satellite observations, EM27/SUN ground-based measurements, HYSPLIT backward trajectory analysis, and the MEIC emission inventory. This study thus jointly analyzes the spatiotemporal variability of atmospheric column-averaged dry-air mole fraction of CO_2 (XCO_2) and CH_4 (XCH_4) and their driving mechanisms, thereby improving the understanding of urban-scale GHG dynamics and their potential implications for other rapidly developing regions.

To bridge the aforementioned knowledge gaps, the overarching aim of this study is to unravel the complex mechanisms driving the spatiotemporal variability of urban GHGs in Hefei, a representative rapidly developing city. Specifically, this study seeks to answer the following core research questions:

(i) What are the long-term trends and seasonal patterns of XCO_2 and XCH_4 in this dynamically evolving urban region?
(ii) To what extent can the diurnal and seasonal co-variations of XCO_2 and XCH_4 be used to decouple the distinct contributions from anthropogenic emissions and biogenic activities?
(iii) How do regional atmospheric transport and local sectoral emissions interact to control these GHG variations?

To answer these questions, we integrate multi-platform observations, including decade-long satellite data and high-resolution ground-based measurements, with backward trajectory modeling and emission inventory analysis. Ultimately, the present study aims to provide a comprehensive framework for understanding GHG dynamics, offering critical scientific insights for targeted emission mitigation strategies in similar rapidly developing regions.

2. Materials and methods

2.1. Data sources and description

The Japan Aerospace Exploration Agency launched GOSAT on January 23, 2009. It is in a sun-synchronous orbit at about 666 km altitude, with a global revisit cycle of three days. GOSAT has two instruments to observe the worldwide distribution of GHGs: the Cloud and Aerosol Imager and the Thermal and Near-infrared Sensor for Carbon Observation.

Besides the Level 3 column-averaged mixing ratios, the daily Level 2 products of XCO_2 and XCH_4 from the Thermal and Near-infrared Sensor for Carbon Observation using the Atmospheric CO_2 Observations from Space (ACOS) retrieval algorithm are available at https://data2.gosat.nies.go.jp/index_en.html. In this study, we analyzed the calibrated XCO_2 data from 2009 to 2020 to characterize its interannual, seasonal, and monthly variations.

The XCO_2 retrieval precision is 1.0–1.5 ppm for one sounding. Regional and global biases are generally less than 0.1–0.5 ppm. For Hefei, we selected GOSAT observations within a region of approximately 1.5° centered on Hefei.

The HYSPLIT model, developed by the United States National Oceanic and Atmospheric Administration and the Environmental Protection Agency, is widely used to analyze air mass trajectories and dispersion. The backward trajectories were clustered to quantify the complexity of air mass transport over Hefei. This is a statistical method that classifies a set of spatially distributed trajectories into a finite number of clusters based on similarity through a hierarchical agglomerative algorithm. It provides an objective classification of the dominant transport pathways of air masses.

Anthropogenic CO_2 emissions were obtained from MEIC version 2.0 by Tsinghua University (http://meicmodel.org.cn/#firstPage). MEIC is a bottom-up emission inventory covering five sectors: power, industry, residential, transportation, and agriculture. It provides monthly emission data at a spatial resolution of 0.25° × 0.25° for 10 key atmospheric species, such as SO_2, NO_X, and CO_2. CO_2 emission calculations are based on the 2006 Intergovernmental Panel on Climate Change Guidelines for National Greenhouse Gas Inventories. The accuracy of MEIC is further improved through the localization of key parameters, calorific value, carbon content, and oxidation ratios, based on provincial-level GHG inventories and on-site measurements in China.

2.2. Greenhouse gas column concentration retrieval method

The ground measurements of trace gases were conducted using an EM27/SUN spectrometer (Bruker Corporation, Germany) for XCO_2 and XCH_4. The Fourier transform infrared instrument (Bruker Corporation, Germany) was located at the Hefei site (31°54'N, 117°10'E, 29 m above sea level), adjacent to a lake in flat terrain. It is part of the Anhui Institute of Optics and Fine Mechanics, operated by the Laboratory of Atmospheric Optics, Chinese Academy of Sciences (Figure 1A).

The research team installed the instrument (Figure 1B), which consists of a Bruker EM27 spectrometer (Bruker Corporation, Germany) and a solar tracker (Bruker Corporation, Germany), in 2018. The instrument achieves an optical path difference of 1.8 cm with a maximum spectral resolution of 0.5 cm^{-1}. Under ideal conditions (sunny days and a stable atmosphere), the standard deviations of XCO_2 and XCH_4 are 0.2 ppm and 2×10^{-3} ppm, respectively.

The long-term comparison results with the global benchmark network, the Total Carbon Column Observing Network, show that XCO_2 differences range from 0.1 to 0.8 ppm (with relative differences of approximately 0.02–0.2%), and XCH_4 differences range from 2×10^{-3} to 8×10^{-3} ppm (with relative differences of approximately 0.1–0.4%).

In the present study, both the ground-based inversion algorithm (profile fitting method) and the satellite

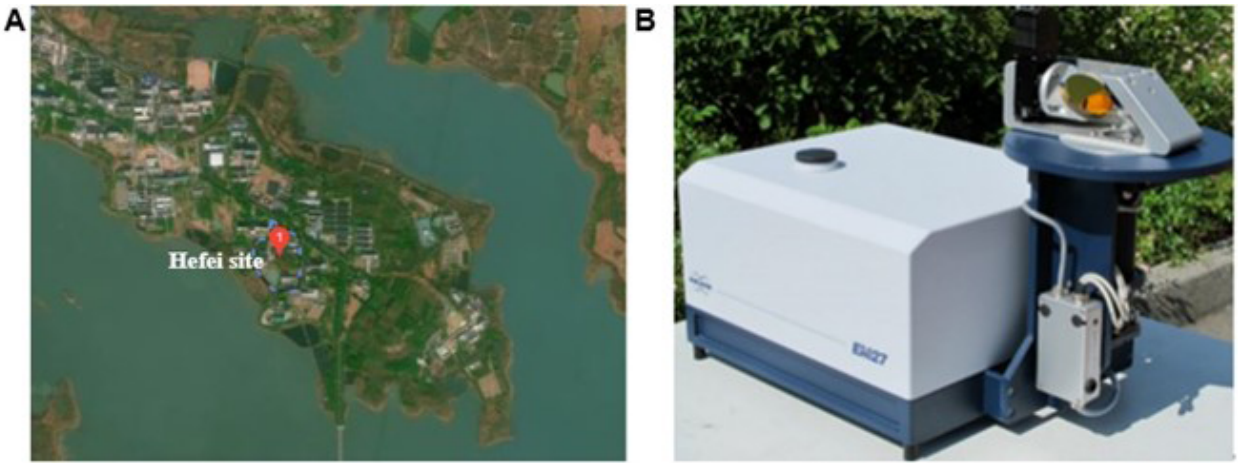

Figure 1. Observation site and instrumentation. (A) Hefei Meteorological Observatory. (B) Fourier transform infrared spectrometer (EM27/SUN).

inversion algorithm (ACOS) use an approximation of the physics of the measurement process. The cost function for retrieving the state vector x consists of two parts: the observation term and the prior constraint term, as shown in **Equation 1**:

$$\chi^2(x) = [y - F(x,b)]^T S_\varepsilon^{-1}[y - F(x,b)] + [x - x_a]^T S_a^{-1}[x - x_a] \quad (1)$$

where y is the observation vector (the Fourier spectrometer measurement), $F(x, b)$ is the forward model, x is the state vector, including parameters such as surface pressure, temperature profile, and XCO_2, x_a is the prior state vector, and S_ε and S_a are the covariance matrices of observation error and a priori error, respectively. Using the Levenberg–Marquardt method for iterative updates:

$$x_{i+1} = x_i + [(1+g)S_a^{-1} + K_i^T S_e^{-1} K_i]^{-1} \times \left\{K_i^T S_e^{-1}[y - F(x_i)] - S_a^{-1}[x_i - x_a]\right\} \quad (2)$$

where, x_i and x_{i+1} are the state vectors, γ is a damping factor, and K_i is the Jacobian matrix:

$$K_i = \frac{\partial F}{\partial x}|_{x=x_i} \quad (3)$$

The iteration proceeds until convergence is achieved, yielding the optimal posterior estimate of the state vector. To evaluate the uncertainty of the inversion results, the posterior error covariance matrix is calculated:

$$\hat{S} = (S_a^{-1} + K^T S_\varepsilon^{-1} K)^{-1} \quad (4)$$

To remove the effects of surface pressure variation, the column-averaged dry air mole fraction (column concentration) is defined in **Equation 5**, using the column abundance of O_2 as a reference to reduce systematic errors:

$$X_{gas} = 0.2095 \times \frac{Column_{gas}}{Column_{O_2}} \quad (5)$$

where column gas and column O_2 are the column abundances of the retrieved gas and O_2, respectively.

The ACOS algorithm uses a multilayer perceptron (MLP) neural network model for calibration:

$$\Delta X_{bias} = MLP(z)$$
$$X_{corrected} = X_{ret} - \Delta X_{bias} \quad (6)$$

where z is the input feature vector of the neural network. There is a systematic deviation between the initial XCO_2 obtained from inversion (denoted as X_{ret}) and the foundational inversion.

2.3. Data analysis and statistical methods

To evaluate the temporal dynamics and source characteristics of atmospheric GHGs, statistical analyses using OriginPro 9 (OriginLab Corporation, USA) were conducted, focusing on long-term trends and inter-species relationships.

2.3.1. Quantification of long-term trends and annual growth rates

To quantify the interannual growth rates and characterize long-term temporal trends of the GHGs, ordinary least squares (OLS) linear regression analyses were applied to the time series of CO_2 and CH_4 concentrations. In these models,

time (years) was set as the independent variable, whereas gas concentration was used as the dependent variable. The slope of the resulting linear regression line directly represents the annual growth rate (ppm/year for CO_2 and CH_4), providing a quantitative metric of atmospheric accumulation. The coefficient of determination (R^2) and the associated slope were utilized to assess the goodness-of-fit and the magnitude of the annual growth rates of CO_2 and CH_4.

2.3.2. Co-emission analysis and enhancement ratios

To identify the co-emission characteristics of CO_2 and CH_4, the linear relationship between the concentrations of these two gases was examined. Pearson correlation coefficients (r) were initially calculated to evaluate the synchronicity of their variations, which typically indicates shared emission sources or similar atmospheric influences. Furthermore, linear regression analysis was performed—with XCO_2 as the independent variable and XCH_4 as the dependent variable—to derive the enhancement ratio ($\Delta XCH_4/\Delta XCO_2$). The slope of this regression serves as an empirical enhancement ratio. Because distinct emission sources (e.g., fossil fuel extraction/combustion, biomass burning, and biological emissions) exhibit different theoretical enhancement ratios, this derived slope acts as a critical emission signature (tracer) for inferring the dominant source sectors contributing to the regional GHG variations.

Furthermore, given the relatively small number of data points in our observational series, standard linear regression is prone to overfitting, which can lead to artificially inflated or spurious goodness-of-fit values. To account for this limitation and avoid overestimating the models' explanatory power, the adjusted R^2 was calculated by incorporating a mathematical penalty based on the degrees of freedom. The adjusted R^2 provides a more conservative and statistically robust evaluation of the linear fits. The specific degrees of freedom for each model were explicitly specified to ensure the reliability of the statistical inference.

3. Results and discussion

3.1. Interannual variations of XCO_2 and XCH_4 column concentrations over Hefei based on GOSAT observations

In this section, we present the spatiotemporal features of the GHG column concentrations over Hefei from 2009 to 2020, based on the GOSAT satellite retrieval products of XCO_2 and XCH_4, and discuss potential confounding factors influencing the spatiotemporal distribution and seasonal variation trends.

As illustrated in Figure 2A, from 2009 to 2020, the global XCO_2 increased from 385.61 to 410.60 ppm, with an average annual increase of 2.23 ± 0.062 ppm/year (Table 1), mainly due to net anthropogenic emissions from fossil fuel combustion and land-use change. Although the annual growth rate varies interannually, the upward trend is maintained.

However, XCO_2 is higher in Hefei than the global average (Figure 3A). The local concentration increased from 388.12 ppm in 2009 to 414.82 ppm in 2010. Thus, the local average annual increase during this period was higher at 2.41 ± 0.074 ppm/year (Table 1). This indicates that XCO_2 increases faster in Hefei than the global average trend.

This may be explained by two main factors. First, as a fast-developing provincial capital and one of the sub-center cities in the Yangtze River Delta urban agglomeration, Hefei has high energy consumption, intensive transportation, and strong urban metabolic activity,[32] creating a strong local source of CO_2. Second, the limited carbon sink capacity in the urban area implies that vegetation's photosynthetic uptake is insufficient to compensate for the high level of anthropogenic emissions, resulting in a positive net carbon flux at the local scale. These findings suggest that cities are anthropogenic CO_2 emission hotspots and thus call for stronger local mitigation actions toward carbon neutrality through regional cooperative governance along atmospheric transport pathways.

After CO_2, CH_4 is the second most important anthropogenic GHG contributing to global warming and accounts for almost one-fourth of the observed global warming since the Industrial Revolution. Figure 2B shows XCH_4 over Hefei compared with the global average for 2009–2020. Due to its reactive nature, the abundance of XCH_4 depends on emissions, transport, deposition, and chemical reactions.

Globally, XCH_4 increased in a linear and steady manner, from 1.762 ppm in 2009 to 1.841 ppm in 2020 (Figure 3B), with an average annual growth rate of $0.00701 \pm 1.55 \times 10^{-4}$ ppm/year (Table 2). Although the Hefei region shows a similar local long-term trend of XCH_4, it exhibits considerable interannual variations (Figures 2 and 3). The net increase was about 72×10^{-3} ppm locally (Figure 3B), and the average annual growth rate was slightly higher than the global rate at $0.00734 \pm 7.42 \times 10^{-4}$ ppm/year (Table 2).

The Hefei regional time series showed accumulation peaks in 2012 and 2016 for different reasons. The 2012 peak is related to high local anthropogenic activity. From 2012 to 2013, coal consumption and production in Anhui Province reached the highest level, and approximately 900

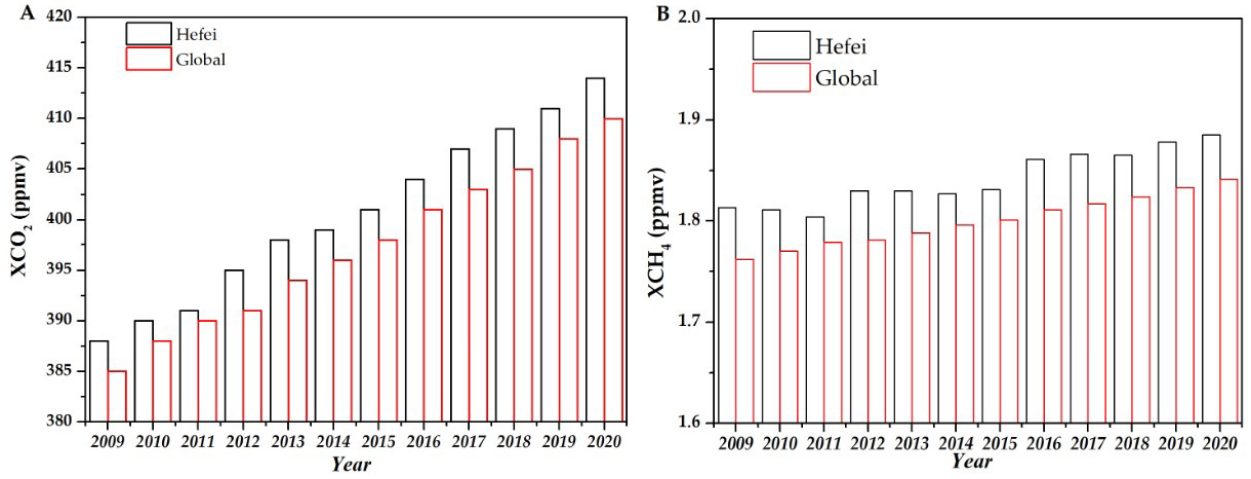

Figure 2. Interannual trends of global and Hefei (A) XCO_2 and (B) XCH_4 column-averaged dry-air mole fractions from 2009 to 2020
Abbreviations: XCH_4: Column-averaged dry-air mole fraction of methane; XCO_2: Column-averaged dry-air mole fraction of carbon dioxide.

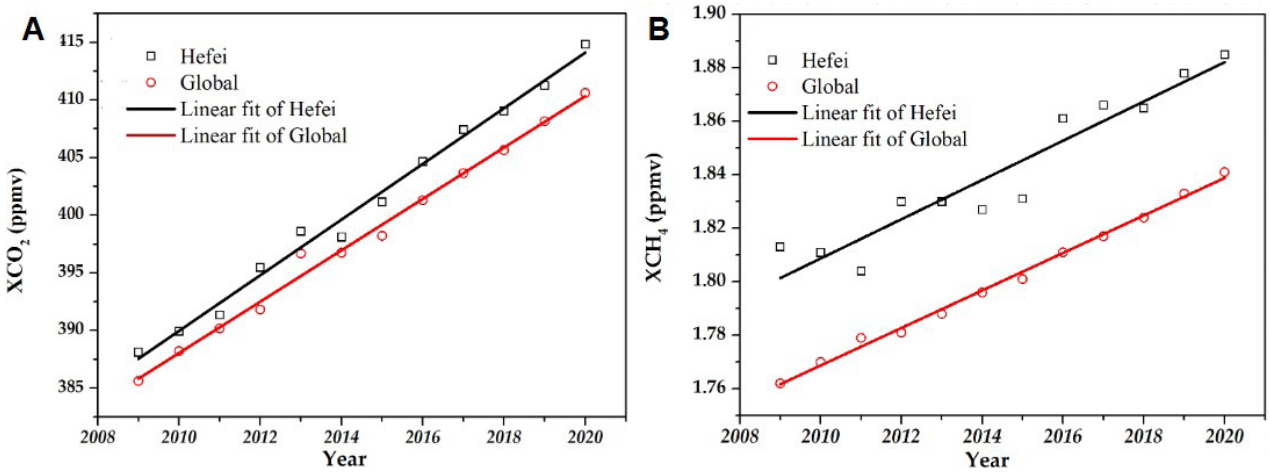

Figure 3. Linear fits for Hefei and global (A) XCO_2 and (B) XCH_4 column-averaged dry-air mole fractions
Abbreviations: XCH_4: Column-averaged dry-air mole fraction of methane; XCO_2: Column-averaged dry-air mole fraction of carbon dioxide.

Table 1. Linear regression statistics and evaluation parameters for XCO_2

Location	Residual sum of squares	*r*	Adjusted R^2 (df = 10)	Slope (ppm)	Standard error
Hefei	7.93	0.995	0.989	2.41	0.074
Global	5.47	0.996	0.992	2.23	0.062

Notes: The table presents ordinary least squares regression results. The reported parameters include the slope, standard error, Pearson's correlation coefficient (*r*), coefficient of determination (R^2), and degrees of freedom (df) for each model. The R^2 values are provided to assess the goodness of fit of the linear regression models.
Abbreviation: df: Degrees of freedom.

Table 2. Linear regression statistics and evaluation parameters for XCH_4

Location	Residual sum of squares	*r*	Adjusted R^2 (df = 10)	Slope (ppm)	Standard error
Hefei	7.88×10^{-4}	0.952	0.898	0.00734	7.42×10^{-4}
Global	3.42×10^{-5}	0.998	0.995	0.00701	1.55×10^{-4}

Notes: The table presents ordinary least squares regression results. The reported parameters include the slope, standard error, Pearson's correlation coefficient (*r*), coefficient of determination (R^2), and degrees of freedom (df) for each model. The R^2 values are provided to assess the goodness of fit of the linear regression models.
Abbreviation: df: Degrees of freedom.

additional production units came into operation in 2012. At that time, the industrial structure was relatively heavy, with six high-energy-consuming industries accounting for 85.4% of the province's industrial energy. In addition, waterlogging may have created anaerobic conditions, thereby increasing CH_4 emissions from wetlands and paddy fields.

In contrast, although increased emissions were linked to extreme climatic conditions at the time, natural emission sources dominated in 2016. That year brought anomalous weather to Anhui Province, which received its highest annual precipitation since 1961, totaling 1,661 mm. Precipitation in autumn was exceptionally high, and farmland and soil were severely waterlogged throughout the province. Waterlogging-induced anaerobic conditions enhanced CH_4 emissions from wetlands and paddy fields. On the other hand, July and August were abnormally warm. The period from July 20 to August 20 was the second warmest on record in the city, favoring biogenic CH_4 production.

Preliminary backward trajectory analysis showed that the heavily elevated CH_4 conditions during autumn in Hefei were mainly associated with air masses originating from local or northern directions, indicating poor ventilation, stagnation, and regional accumulation during this season. Therefore, under weakly ventilated autumn conditions, and in contrast to winter atmospheric dynamics, enhanced regional accumulation suggests a strong contribution from local sources and complex atmospheric transport processes, as elaborated in Section 3.4.

3.2. The seasonal variation of column concentrations of greenhouse gases CO_2 and CH_4

The column-averaged concentrations reflect the seasonal sum of anthropogenic and natural cycles, since both emissions and sinks of CO_2 and CH_4 are dynamic. Indeed, several human-induced activities, such as combustion, and natural processes (e.g., vegetation photosynthesis and respiration), act as key drivers of seasonal variability in atmospheric CO_2 and CH_4 through concurrent emissions and removal processes.[24,26]

The heating season requires higher consumption of coal and oil in winter than in summer, thus producing more CO_2 during the winter heating period. However, sources and sinks vary seasonally and thus determine the total atmospheric burden and distribution of these gases, driving variations in the strength of the greenhouse effect on a planetary scale over time.[28]

Hence, the seasonal development of the Earth's surface temperature represents another critical feedback mechanism influencing the greenhouse effect. Temperature changes driven by the seasonally varying Earth–Sun geometry—changes in Earth's position relative to the Sun that alter the energy received at the top of the atmosphere—affect the concentrations and radiative properties of the main GHGs CO_2, CH_4, and water vapor.[27] In this sense, this mechanism implies an additional positive feedback in the greenhouse system.

Several recent studies, emphasizing the interaction between seasonal cycles and large-scale climate dynamics, report that global warming induced by an enhanced greenhouse effect destabilizes the climate and raises the likelihood of extreme seasonal events, such as heatwaves, droughts, and heavy precipitation. Heatwaves occur primarily in summer, while cold surges and heavy snowfall typically characterize winter.[28] Such altered event regimes will influence habitat types, ecological conditions, crop production, and human life.

These secular and seasonal GHG forcings are continuously mixed and transported within the atmosphere across multiple temporal scales, from instantaneous to seasonal variability. Stable weather conditions and temperature inversions—typical of atmospheric conditions during winter—can easily trap pollutants and enhance

GHG concentrations, especially those emitted from comparatively local sources such as residential heating.[31]

During summer, thermally generated turbulence will enhance atmospheric mixing and dilution; however, this does not necessarily imply lower background levels. Pure or typical seasonal behavior is increasingly influenced by overlapping factors, including long-term global climate change, regional economic activity, and complex geographic conditions. Thus, large spatial and interannual variability appear in GHG concentrations across different stations.

Hefei is located in a subtropical humid-monsoon climate zone, with strong seasonal variability reflected in changes in ecology, agriculture, and human activity throughout the year.[32] Hence, spring is from March to May, summer from June to August, autumn from September to November, and winter from December to February. To quantify the seasonal growth rates, independent simple linear regression models were applied separately to the data for each season, with time (year) acting as the sole independent variable. It should be explicitly noted that because these are separate univariate regressions rather than a single multivariable model, issues of multicollinearity are not applicable.

Figure 4 presents the resultant long-term seasonal trends for XCO_2 over Hefei during 2010–2020. Although the overall dataset spans 2009–2020, the seasonal analysis was restricted to 2010 onward because complete monthly data for a full annual cycle (January–December) were not available for 2009. Linear regression analyses on these datasets show consistent and statistically significant upward trends across all seasons. The rates of annual increase are highly similar across winter, spring, and autumn. On the other hand, the interannual variability is significantly higher during summer, as reflected in a substantially lower R^2 relative to the fits in other seasons. Indeed, winter, spring, and autumn regressions exhibit strong linear increases, as indicated by $R^2 > 0.95$. Hence, the findings reveal a persistent increase in XCO_2 over the study region across all four seasons year after year.

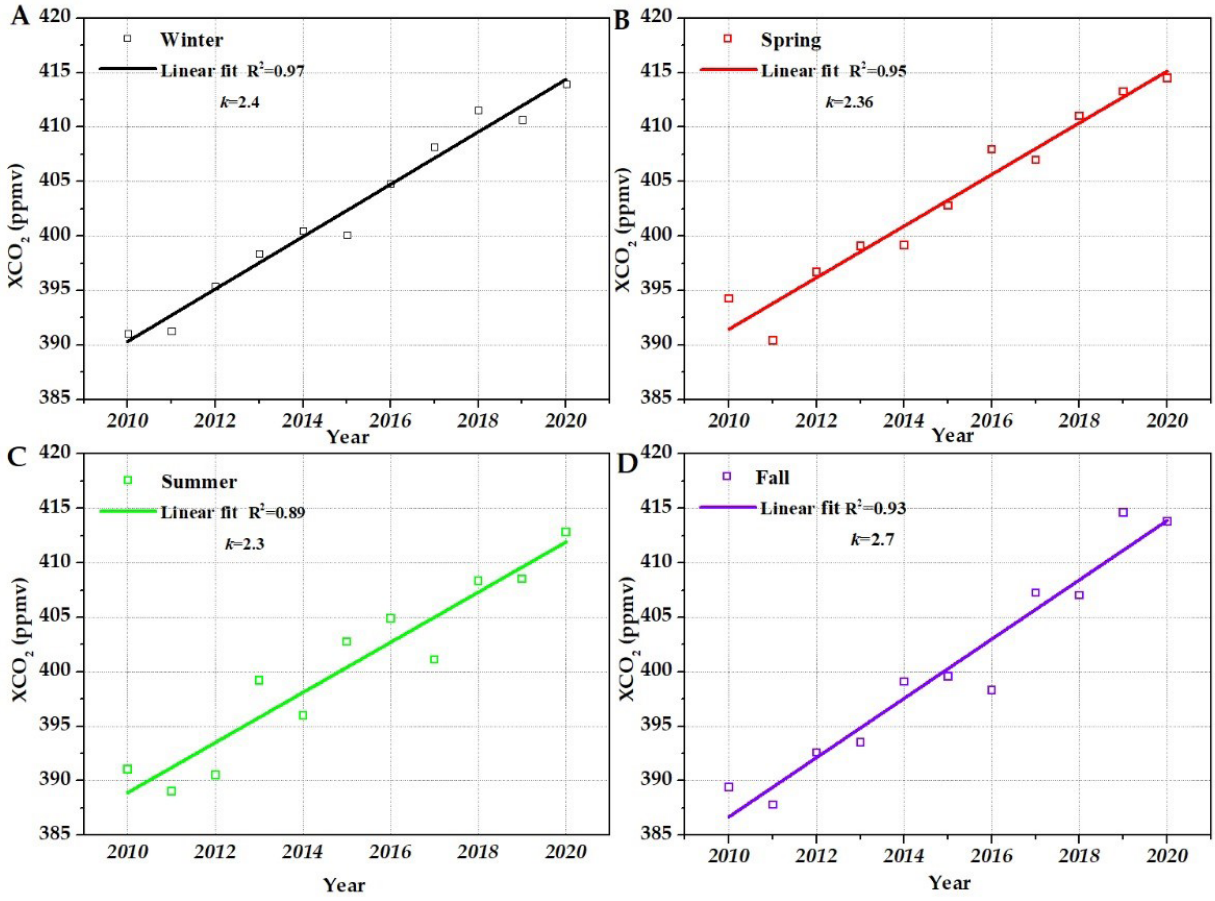

Figure 4. Seasonal trends of the column-averaged dry-air mole fraction of carbon dioxide (XCO_2) from 2010 to 2020 in Hefei: (A) Winter, (B) spring, (C) summer, and (D) fall.

On average, based on linear regression results, the spring, summer, and winter annual growth rates of XCO_2 are on the order of 2.3 ± 0.18 ppm/year, while in autumn the rate exceeds 2.7 ± 0.2 ppm/year. The significantly higher increase in autumn suggests that unique autumn-related causes may explain the stronger increases than the other seasons, whereas different regional anthropogenic emission patterns, especially those involving atmospheric transport during autumn, also likely influence this season.

The regional and local characteristics of XCO_2 were influenced by the combined effects of anthropogenic and natural activities. Within this context, summer is dominated by the surge in active biosphere photosynthesis, which is a strong internal loss term for atmospheric CO_2. The winter season is therefore the opposite phase; the photosynthesis sink is minimal, and anthropogenic emissions from dense residential heating add to atmospheric CO_2 levels, both processes increasing the gross amount of atmospheric CO_2 during the cold season.

The seasonality of atmospheric XCH_4 in Hefei over the period 2010–2020 is shown in Figure 5, where both seasonal and interannual trends are presented. In particular, the atmospheric column concentration over Hefei shows elevated levels in summer and autumn while being suppressed during winter and spring.

During the winter and spring seasons, the atmospheric boundary layer is generally shallow and stable, creating a poor mixing environment at higher altitudes. Moreover, northerly and northwesterly winds during winter also bring air masses further inland and out of the country, thus clean continental air may be advected toward the Hefei region, partially compensating for local source emissions and diluting them in winter and spring.

In summer, convective conditions dominate and a deep atmospheric boundary layer forms, allowing for good vertical mixing of emitted species. Air masses arriving in the region in summer are most strongly influenced by air transported inland from the south, characterized by

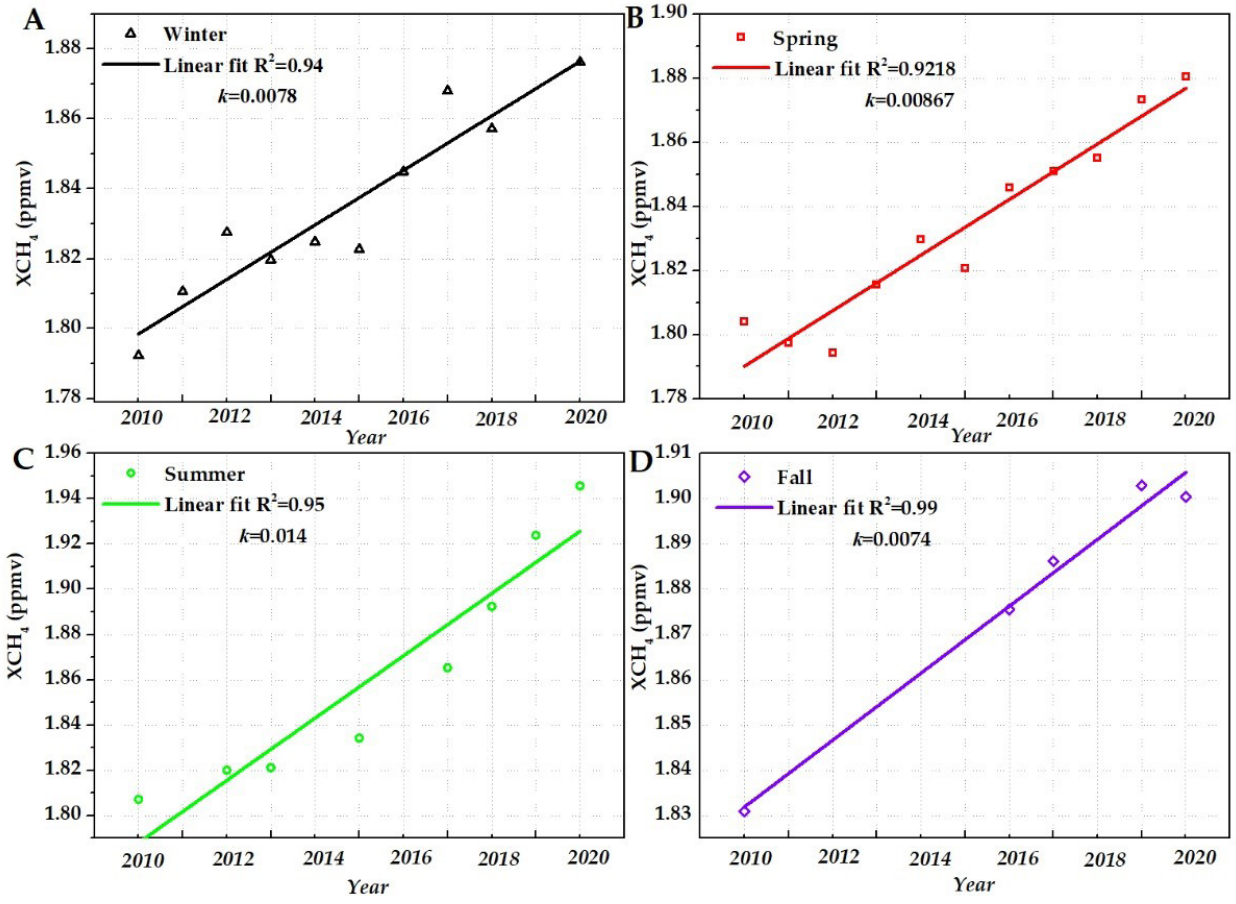

Figure 5. Annual trends of the column-averaged dry-air mole fraction of methane (XCH_4) from 2010 to 2020 in Hefei: (A) Winter, (B) spring, (C) summer, and (D) fall.

higher humidity and predominant agricultural activity. A first assessment of air mass histories based on backward trajectory modeling is presented in Section 3.4.

Regression analysis for the four seasons shows R^2 coefficients above 0.92, suggesting a good fit to the annual increase, despite some concern about the fit quality in autumn due to the limited data. Despite the amplitude of the seasonal cycle, the concentration of atmospheric XCH_4 over Hefei exhibits a clear year-to-year increase. This increase occurs for all seasons but at different rates and variabilities. The smaller growth rate periods are winter and autumn. Summer shows the highest growth rates, with an average annual increase in XCH_4 of 0.014 ± 0.0019 ppm/year (Table 3). The summer growth rate (k = 0.014) was nearly twice as high as in other seasons. This accelerated summer accumulation strongly suggests the presence of progressively intensifying, season-specific emission sources. It is likely driven by temperature-dependent methanogenesis from regional wetlands or agricultural activities (e.g., paddy fields), which are highly sensitive to the warmer and wetter conditions typical of the summer months.

Thus, in the preceding sections, long interannual and seasonal trends for satellite-observed XCO_2 and XCH_4 column amounts over Hefei were obtained. While this analysis provides a regional-scale overview of the temporal evolution of these two GHGs, satellite observations—due to their revisit nature—are not capable of resolving high-frequency diurnal and short-term day-to-day variability. Such information is crucial when accurately characterizing detailed atmospheric transport and local emission responses, especially during dynamic periods such as the spring transition.

3.3. Short-term variation characteristics of XCO_2 and XCH_4 over Hefei based on EM27/SUN observations

An independent ground-based measurement dataset collected in March and April 2018 using the EM27/SUN portable FTS is also used to complement the aforementioned limitations and further characterize the short-term variability of GHGs. The use of the EM27/SUN instrument in a network for satellite validation offers a good combination of portability and spatiotemporal resolution, enabling the capture of diurnal variations and short-lived anomalies. The present dataset thus provides a basis for satellite validation and process-level analysis. Therefore, this section examines the diurnal variability of XCO_2 and XCH_4 during the spring season based on EM27/SUN observations.

In March and April 2018, ground-based FTS observations were newly established in Hefei. Section 2 presents a technical overview of this system. Favorable meteorological conditions prevailed during the observation period, characterized by generally clear skies and low variability in atmospheric conditions. According to the quality control procedure for ground-based FTS, all spectra with relative solar intensity changes greater than 5% for a given measurement period are rejected. Thus, after quality control filtering and post-processing, the resulting XCO_2 and XCH_4 datasets were found suitable for analyzing diurnal variability, as shown in Figure 6.

Table 3. Statistical analysis of linear regression parameters for seasonal annual mean values of XCO_2 and XCH_4

Season	Residual sum of squares		r		Adjusted R^2 (df = 10)		Slope (ppm/year)		Standard error	
	XCO_2	XCH_4	XCO_2	XCH_4	XCO_2	XCH_4	XCO_2	XCH_4	XCO_2	XCH_4
Spring	30.82	6.27×10^{-4}	0.98	0.96	0.95	0.92	2.4	0.0087	0.176	7.96×10^{-4}
Summer	63.10	0.00191	0.95	0.95	0.89	0.88	2.3	0.014	0.252	0.00188
Fall	53.48	5.74×10^{-5}	0.97	0.99	0.93	0.98	2.7	0.0074	0.232	5.59×10^{-4}
Winter	15.57	7.21×10^{-4}	0.98	0.94	0.97	0.87	2.4	0.0078	0.125	9.88×10^{-4}

Notes: The table presents ordinary least squares regression results. The reported parameters include the slope, standard error, Pearson's correlation coefficient (r), coefficient of determination (R^2), and degrees of freedom (df) for each model. The R^2 values are provided to assess the goodness of fit of the linear regression models.

Abbreviations: df: Degrees of freedom. XCH_4: Column-averaged dry-air mole fraction of methane; XCO_2: Column-averaged dry-air mole fraction of carbon dioxide.

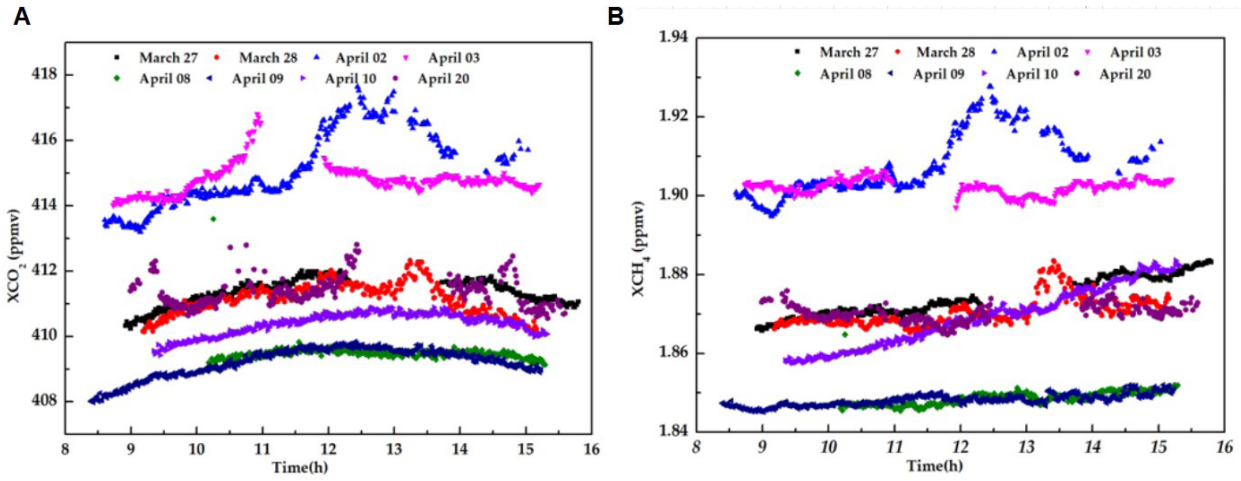

Figure 6. Diurnal variations of (A) XCO_2 and (B) XCH_4 in 2018
Abbreviations: XCH_4: Column-averaged dry-air mole fraction of methane; XCO_2: Column-averaged dry-air mole fraction of carbon dioxide.

On the other hand, the diurnal variability analysis of the XCO_2 and XCH_4 columns showed clear day-to-day differences during the full period from March 2018 to April 2018. For instance, April 8–9 was characterized by low column values compared to the higher values observed on April 2–3. One important feature highlighted in the column variability was that daily change patterns were at times similar. Similarities were observed, for example, between March 28 and April 2. This may indicate that the variability observed was associated with similar emission sources and/or atmospheric transport processes. On March 28, XCO_2 and XCH_4 showed diurnal behavior with a maximum around midday (12:30 h), which then rapidly decreased to its minimum at about 14:00 h and then slowly increased again. Under the prevailing southerly wind conditions on March 28, the measurement site was downwind of the urban area in the afternoon and was thus possibly influenced by urban anthropogenic emissions after local noon. On a few other days, weather conditions were poor, thereby limiting data availability. For instance, although data for March 27 are presented in Figure 6 and Table 4, a substantial portion of these data were deemed invalid due to poor observational conditions. Similarly, partial data coverage occurred on April 3 and April 20. This discontinuous nature of the dataset increases the difficulty of interpreting diurnal variability.

As presented in Table 4, ΔXCO_2 in the daily profile varied from 1.469 to 4.59 ppm, with a mean ΔXCO_2 value of 2.67 ppm. This indicates that the profiles varied significantly in shape from day to day, suggesting that surface source–sink processes associated with vegetation may operate on relatively long timescales at the Hefei measurement site. XCH_4 varied only slightly, with ΔXCH_4 ranging between 0.0068 ppm and 0.0329 ppm and a mean value of 0.0179 ppm over the observation period. Thus, a relatively stable background was observed on most days, with a few more strongly variable days (for instance, April 2 and April 10). In particular, April 2 exhibited the largest variability (0.0329 ppm), which corresponds to 1.7% of the daily mean value. This may be attributed to strong regional advection and/or enhanced local emission sources influencing CH_4 variability. The day with the largest XCO_2 variability (approximately 4.59 ppm) was April 8, corresponding to 1.12% of the average value. Variations of this magnitude may reflect strong surface exchange processes or changes in meteorological conditions.

Statistical values of the day-to-day variations in XCO_2 and XCH_4 are presented in Table 5. Standard deviations of within-day diurnal variations in XCO_2 over the observation period are generally on the order of 10^{-1} ppm, except on April 2. Excluding this day, diurnal variability in column-averaged dry-air mole fraction was generally small during the observation period. Mean, minimum, and maximum daily average XCO_2 values were 411.59, 409.22, and 415.05 ppm, respectively. Similarly, diurnal variations in XCH_4 were relatively minor, with standard deviations typically on the order of 10^{-2} ppm. The mean XCH_4 value over the observation period was 1.874 ppm.

Variations of XCO_2 and XCH_4 during the observation period are depicted in Figure 7. The mean XCO_2 ranged between 409 and 416 ppm, with a mean of about 412 ppm. This is several ppm above the global background level during this period (approximately 405–408 ppm), indicating that this urban site in Hefei is influenced by regional anthropogenic emissions.

Meanwhile, XCH_4 ranged between 1.84 and 1.91 ppm, with an average of 1.88 ppm. It is slightly higher than the global background level near 1.85 ppm, likely due to combined contributions from regional and local sources in and around Hefei city. XCO_2 shows pronounced day-to-day variability of nearly 7 ppm, reaching a maximum value of about 416 ppm on April 2, as shown in Figure 7A. XCH_4 shows smaller day-to-day variability (~0.07 ppm; ~3.7% of the mean). Overall, the relative variability of XCH_4 is lower than that of XCO_2.

Table 4. Daily variations of XCO_2 and XCH_4

Date (2018)	ΔXCO_2 (ppm)	ΔXCH_4 (ppm)
March 27	1.770	0.0178
March 28	2.206	0.0184
April 2[a]	4.443[b]	0.0329[b]
April 3	2.797	0.0100
April 8	4.590[b]	0.0193
April 9	1.857	0.0068
April 10	1.469	0.0259[b]
April 20	2.254	0.0119

Notes: [a]Elevated variability in both CO_2 and CH_4 concentrations is observed on these dates. [b]Elevated variability in greenhouse gas concentration is observed.
Abbreviations: XCH_4: Column-averaged dry-air mole fraction of methane; XCO_2: Column-averaged dry-air mole fraction of carbon dioxide.

April 2, which showed an extreme peak in XCH_4, also coincided with the largest daily change in XCH_4 (Table 4). Other features observed on April 2 are analyzed further in Figure 8.

Significant diurnal variations for both XCO_2 and XCH_4 peaked simultaneously in the early afternoon throughout the observation period, as shown in Figure 8. The positive correlation between the diurnal cycles of XCO_2 and XCH_4 suggests co-variation driven by shared atmospheric processes or emission sources. The strong linear correlation of XCO_2 and XCH_4 ($R^2 = 0.965$) in Figure 9 further supports the presence of a dominant co-varying influence affecting both gases simultaneously. The slope ($\Delta XCH_4/\Delta XCO_2 \approx 0.007$) is consistent with a fossil fuel combustion signature, potentially associated with coal combustion and related industrial activities.

In this respect, local anthropogenic combustion sources likely contribute significantly to the observed variability during the observation period. Under certain meteorological conditions, such as stagnant air masses and prevailing southerly winds (e.g., on April 2, when the site was downwind of the urban center), these sources may simultaneously enhance both gases. This case study provides a process-level linkage between local emissions and atmospheric variability, complementing long-term satellite observations with short-term ground-based measurements in an urban environment.

3.4. The driving role of seasonal transport patterns in the trends of greenhouse gas concentration changes

Based on ground-based measurements, a robust dependency has been observed between daily cycles of atmospheric CO_2 and CH_4 concentrations, suggesting that short-term variations in both gases are largely driven by common processes. In particular, human activities with pronounced diurnal cycles are strong candidates for controlling atmospheric concentrations of CO_2 and CH_4. Emissions from morning traffic and solid waste incineration are examples of processes that may co-drive variability in both gases.[31] Likewise, because many environmental parameters influence them simultaneously, biosphere–atmosphere exchange of these gases occurs synchronously with temperature and vegetation activity.

Therefore, spatiotemporal correlations have been increasingly used as a promising metric for process-level interpretation between these two key GHGs. Positive correlations may indicate co-emission from common sources, such as fossil fuel combustion and biomass burning; in contrast, weak or negative correlations may reflect differing source–sink dynamics. For instance, ecosystems such as wetlands act as CH_4 sources while serving as CO_2 sinks through primary production.

At the diurnal timescale, previous studies attribute variability primarily to fast processes, whereas at seasonal timescales, the fundamental drivers shift due to changes in phenology, surface activity, soil microbial processes, and energy consumption.[28] On this basis, a fundamentally different seasonal character in the relationship between these two gases can be expected. Hence, within a modeling framework, seasonal-scale analyses of CO_2–CH_4 correlations provide an important component for understanding source–sink dynamics under varying climatic and ecological conditions.

One of the primary findings of the present study was the strong seasonal dependence of XCO_2 and XCH_4

Table 5. Daily mean and standard deviation of XCO_2 and XCH_4 concentrations

Date (2018)	XCO_2		XCH_4	
	Mean	SD	Mean	SD
March 27	411.34	0.40	1.87	0.00503
March 28	411.15	0.49	1.87	0.00366
April 2	415.05	1.15	1.91	0.00778
April 3	414.79	0.46	1.90	0.00188
April 8	409.47	0.26	1.85	0.00181
April 9	409.22	0.44	1.85	0.00144
April 10	410.38	0.34	1.87	0.00755
April 20	411.36	0.46	1.87	0.00223

Abbreviations: SD: Standard deviation; XCH_4: Column-averaged dry-air mole fraction of methane; XCO_2: Column-averaged dry-air mole fraction of carbon dioxide.

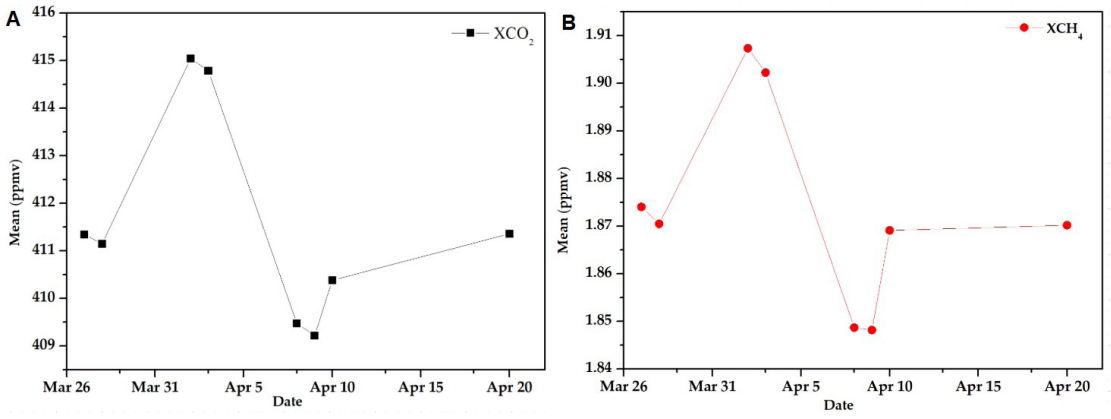

Figure 7. Variations in (A) XCO_2 and (B) XCH_4
Abbreviations: XCH4: Column-averaged dry-air mole fraction of methane; XCO2: Column-averaged dry-air mole fraction of carbon dioxide.

correlations over Hefei (Figure 10 and Table 6). The high R^2 values (>0.86) in spring, autumn, and winter indicate strong positive correlations, suggesting that atmospheric variability in both species is influenced by processes acting synchronously during these seasons, potentially associated with anthropogenic combustion emissions, including coal heating and industrial activities. These sources are spatially co-located and tend to co-vary with meteorological conditions that limit atmospheric dispersion.

During summer, the correlation weakens, with R^2 = 0.66. This decoupling represents a key shift in the dominant driving regime. The East Asian summer monsoon system generally dominates this region in summer (Figure 11B), transporting generally clean marine air masses and thereby diluting anthropogenic signals. At the same time, the onset of the growing season signifies an increasing influence

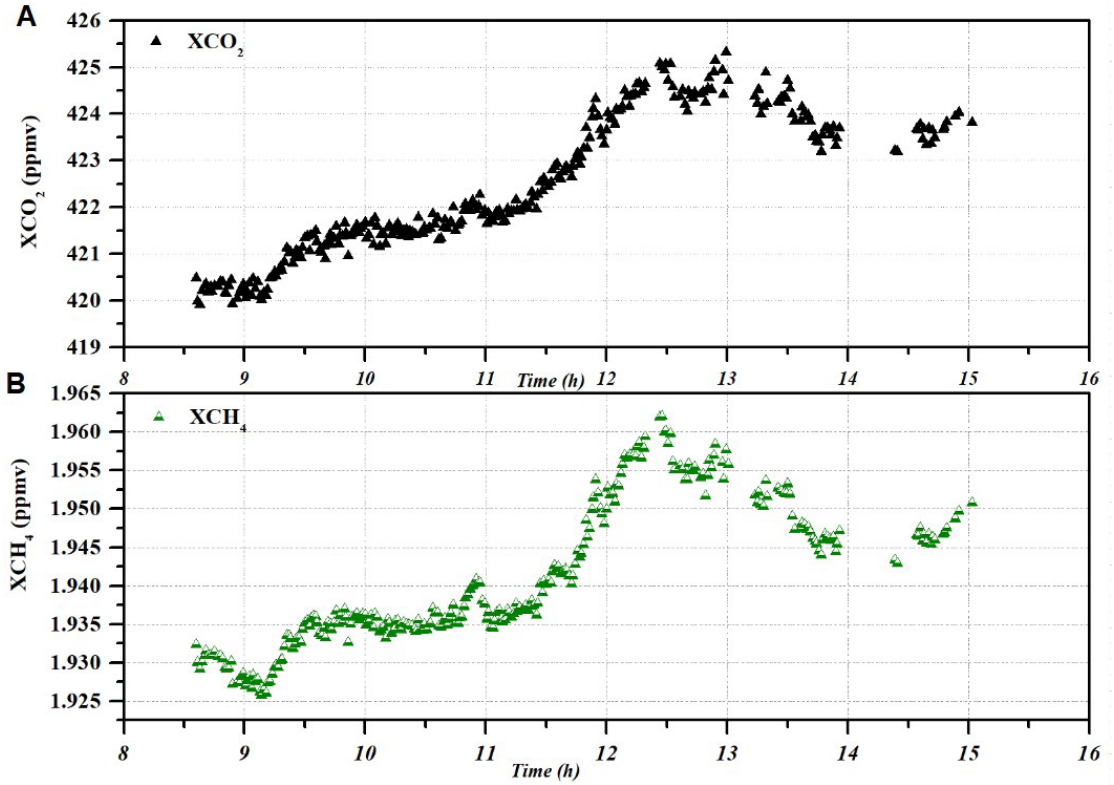

Figure 8. Diurnal variations of XCO_2 and XCH_4 retrieved using a Fourier transform spectrometer on April 2, 2018
Abbreviations: XCH4: Column-averaged dry-air mole fraction of methane; XCO2: Column-averaged dry-air mole fraction of carbon dioxide.

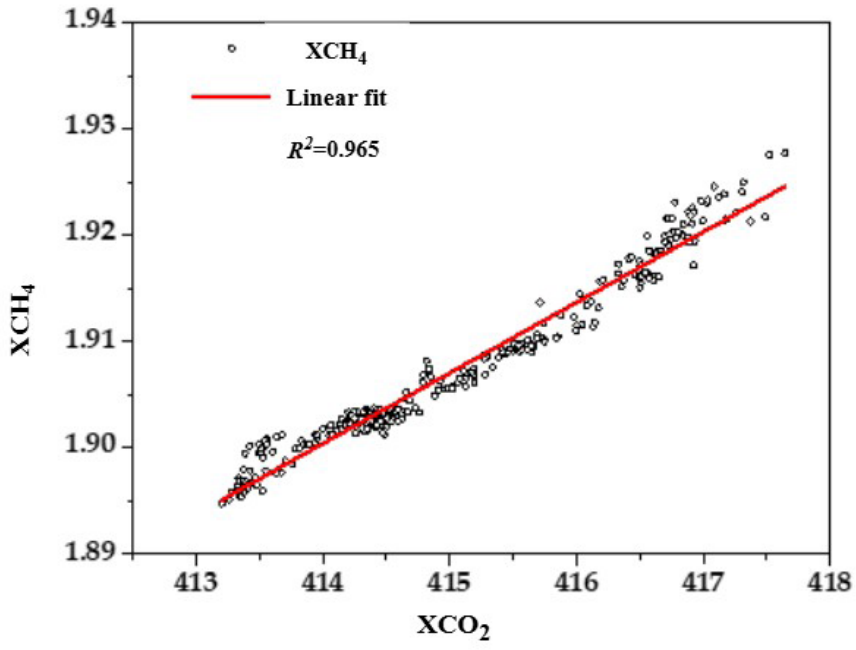

Figure 9. Correlation between XCH_4 and XCO_2 in Hefei on April 2, 2018
Abbreviations: XCH4: Column-averaged dry-air mole fraction of methane; XCO2: Column-averaged dry-air mole fraction of carbon dioxide.

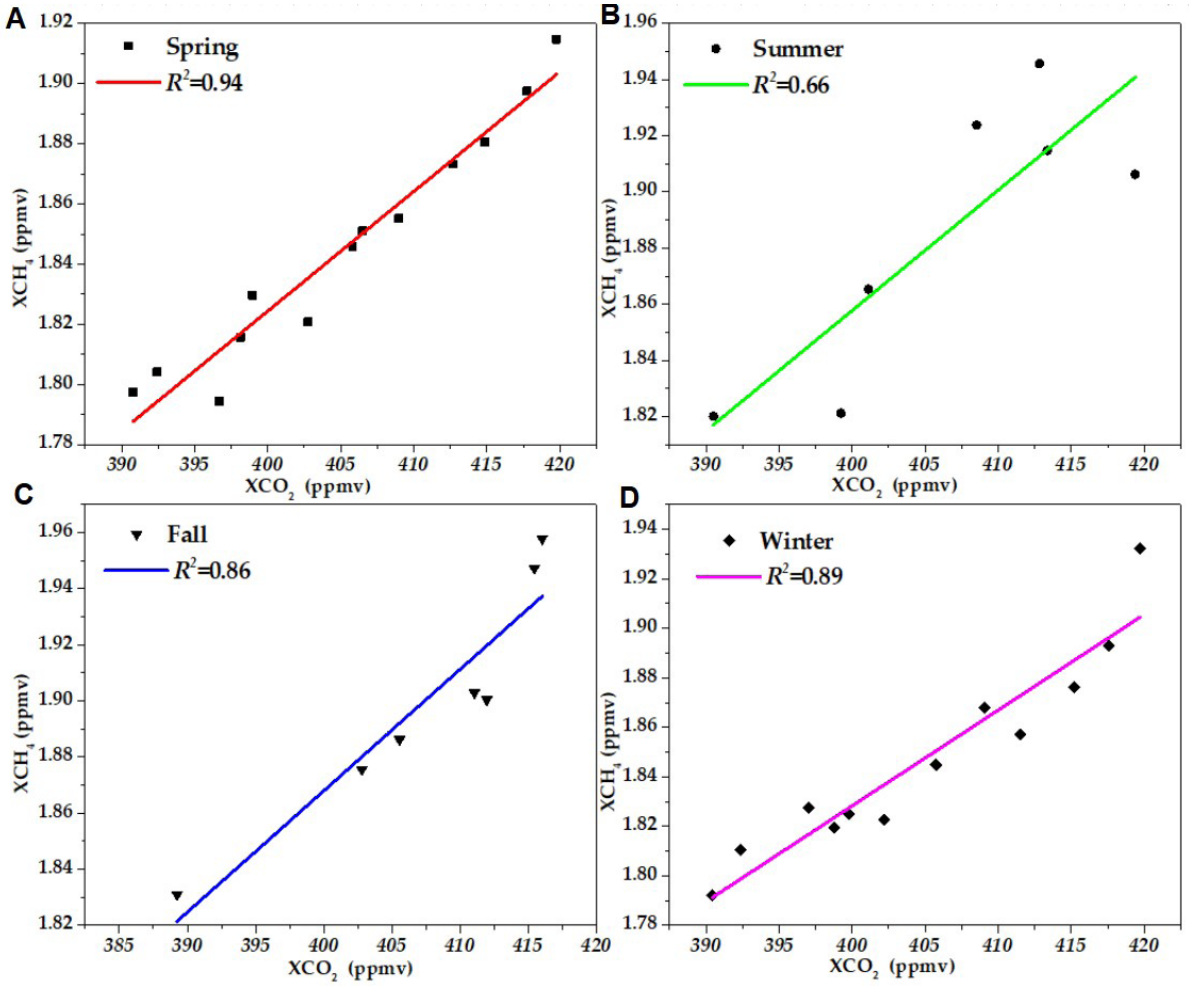

Figure 10. Seasonal correlations between XCO_2 and XCH_4: (A) Spring, (B) summer, (C) fall, and (D) winter.
Abbreviations: XCH4: Column-averaged dry-air mole fraction of methane; XCO_2: Column-averaged dry-air mole fraction of carbon dioxide.

Table 6. Statistical analysis of linear regression between XCO_2 and XCH_4

Season	Residual sum of squares	*r*	Adjusted R^2 (df)	Slope (ppm)	Standard error
Spring	9.71×10^{-4}	0.97	0.94 (13)	0.0040	2.87×10^{-4}
Summer	0.0043	0.85	0.66 (7)	0.0043	0.0012
Fall	0.0013	0.94	0.86 (7)	0.0043	6.90×10^{-4}
Winter	0.0017	0.95	0.89 (12)	0.0039	4.00×10^{-4}

Abbreviation: df: Degrees of freedom.

of biogenic sources and sinks. Enhanced photosynthetic activity leads to strong CO_2 uptake, while flooded rice paddies and warmed summer conditions stimulate increased CH_4 emissions from wetlands and agricultural systems.

Consequently, atmospheric concentrations of both gases tend to diverge, as a CO_2 sink is accompanied by CH_4 emissions, leading to pronounced seasonal changes in the correlation structure. These differences indicate a transition from a combustion-dominated anthropogenic regime during the cold season to a mixed, predominantly biogenic regime during the warm season, in which multiple source processes significantly influence GHG concentrations in the Hefei region. Based on backward trajectory analyses, seasonally distinct transport pathways and source regions further contribute to the observed divergence in XCO_2 and XCH_4 patterns.

The HYSPLIT model was employed to simulate three-dimensional daily 72-hour backward trajectories for 2020 at Hefei (31.51°N, 117.17°E). The year was divided into four seasons: spring (March–May), summer (June–August), autumn (September–November), and winter (December–February). Three arrival heights (500, 1,000, and 1,500 m above ground level) were used to represent different transport layers. Trajectory endpoints were clustered into six groups per season to identify dominant transport pathways and their seasonal variability.

The general seasonal pathway pattern for backward trajectories to Hefei is depicted in Figure 11. Apart from summer, air masses generally arrive from two main pathways: a long-range transport pathway from the industrial–agricultural regions of North China and a local to mid-range pathway from Anhui Province and surrounding areas. In terms of emission typology, these regions represent strong sources of fossil fuel combustion associated with industrial activity and domestic heating, as well as agricultural residue burning. This explains why, during these three seasons, XCO_2 and XCH_4 exhibit enhanced concentrations originating from similar source regions. Accordingly, elevated concentrations of XCO_2 and XCH_4 are linked to similar emission patterns. For example, coal combustion-related activities emit both CO_2 and CH_4 from coal mining, while crop residue burning also releases both gases. Given these multiple co-emission sources, significant positive correlations in their concentrations are expected ($R^2 > 0.8$) (Figure 10).

During summer, the correlation between the two weakens ($R^2 = 0.66$). This seasonal decoupling represents a clear shift in the dominant control regime. In this region, the East Asian summer monsoon transports relatively clean

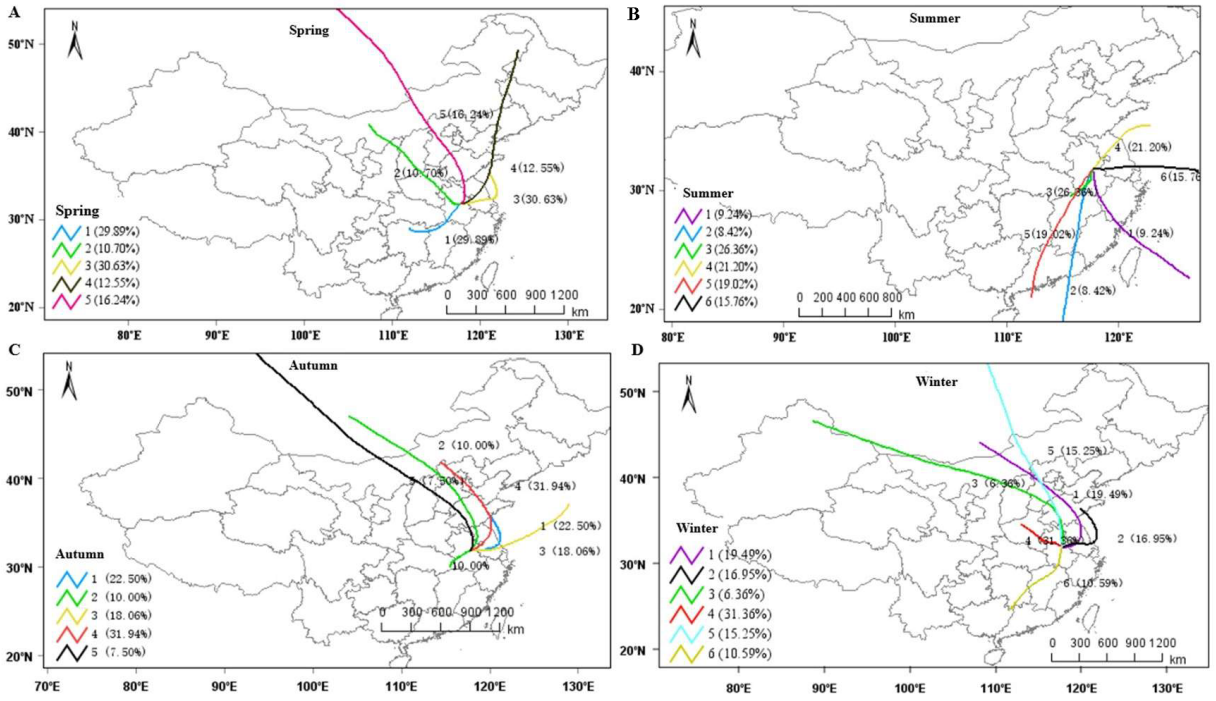

Figure 11. Cluster analysis of 72 h backward trajectories for Hefei in 2020: (A) Spring, (B) summer, (C) autumn, and (D) winter.

marine air masses (Figure 11B), which dilute anthropogenic signals. At the same time, the growing seasons lead to enhanced vegetation photosynthesis, acting as a strong sink for CO_2, while warm conditions and flooded rice paddies promote increased CH_4 emissions from wetlands and agricultural systems. Under these conditions, changes in atmospheric concentrations of the two gases tend to diverge, resulting in weaker correlation. In this context, seasonal changes in correlation patterns reflect a transition from a combustion-dominated anthropogenic regime during the cold season to a mixed regime in which biogenic sources and sinks strongly influence GHG concentrations during the warm season.

The highest annual growth in XCO_2 concentration occurs in autumn (Figure 4 and Table 3). This suggests a period of enhanced coupling between atmospheric transport and emission sources. Airflows from the northwest, particularly clusters 4 and 5 (Figure 11C; with 39.44% frequency), represent a major transport pathway from the North China Plain. This region is active in the post-harvest crop residue burning and sustained industrial activity prior to the onset of northern heating in autumn, thereby providing a significant external input of CO_2. Meanwhile, vegetation photosynthesis weakens in autumn. The combination of transport emissions and reduced biospheric uptake leads to elevated XCO_2 concentrations.

In contrast, XCH_4 exhibits the lowest growth rate in autumn (Figure 5 and Table 3), indicating that distinct transport pathways and source dynamics govern its variability. Although northwesterly airflows can transport CH_4 from biomass burning, these emissions are typically episodic and short-lived. This contrasts with the relatively sustained emissions from rice paddies during summer. In late summer and early autumn, elevated hydroxyl radical concentrations enhance CH_4 oxidation during transport, thereby limiting its accumulation. In addition, local emissions decrease substantially during the paddy harvest period in autumn. As a result, there is no reinforcing effect between transported and local CH_4 sources, and the potential for sustained concentration growth is reduced. Overall, the contrasting seasonal behavior of XCO_2 and XCH_4 reflects species-specific responses to the combined effects of atmospheric transport and local emission processes.

The transport pathway of GHGs through the atmosphere depends, to a large extent, on the temporal stability of their emission sources. For XCO_2, in particular, since the major emission sources are broad and temporally stable—such as industrial, transport, and heating—the influence of transport pathways may primarily manifest as variations in the magnitude of the growth rate. Transport pathways may introduce additional short-term enhancements that are unlikely to affect the long-term trend, which is mainly driven by sustained large-scale anthropogenic emissions.

In contrast, for XCH_4, where emission peaks are strongly seasonal, transport pathways tend to dominate the observed variability in growth rate. This is because medium-range transport in summer (clusters 4 and 5) is spatially and temporally coherent with strong and sustained emissions from paddy fields, thereby contributing to the annual maximum growth rate of XCH_4. In winter, short-range transport is spatially coherent with emissions from heating but corresponds to the lowest growth rate due to stable meteorological conditions that limit atmospheric dispersion. Finally, in autumn, the combination of local and long-range transport, which is temporally mismatched with pulsed emissions from straw burning, results in the lowest growth rate of the year.

These findings support the hypothesis that transport pathways modulate the timing and magnitude of external inputs, interacting with local seasonal emissions to produce the observed seasonal growth pattern of XCH_4.

Additionally, these findings suggest that atmospheric transport pathways are a primary control on the seasonality of the two GHGs in the Hefei region. However, differences in source–sink dynamics result in distinct modes of modulation. The results demonstrated the seasonal correlation between GOSAT satellite-derived XCO_2 and XCH_4 and examined the impact of transport on GHG variability over Hefei. This was achieved using backward trajectory cluster analysis of airflow pathways. Seasonal changes in transport pathway structure are therefore considered important drivers of variability in column-averaged concentrations at the site. However, column density remains an aggregate indicator of source strength, atmospheric conditions, and chemical transport processes that shape ambient concentrations. Hence, source contributions cannot be uniquely attributed based solely on concentration measurements.

3.5. Analysis of the driving mechanisms of anthropogenic emission inventories on greenhouse gas concentration changes

The MEIC inventory of anthropogenic emissions characterizes the source features of GHGs and the spatiotemporal patterns of anthropogenic CO_2 emissions. This provides a robust, physically consistent, and data-driven framework for interpreting observed atmospheric concentrations in relation to ground-level emissions. It strengthens the linkage between atmospheric concentrations and their corresponding emission sources, thereby enabling source attribution and supporting the

evaluation of emission control strategies and mitigation targeting.

Figure 12 shows the evolution of total anthropogenic CO_2 emissions and the share of various economic sectors in total emissions for Hefei during the period of 2009–2020. A fluctuating upward trend was observed in total CO_2 emissions, rising from 151.5 kt in 2009 to 230.0 kt in 2020, indicating a 52% increase. Correlation analysis between the interannual series and the annual average XCO_2 (Figure 4) shows a strong positive correlation (r = 0.71, R^2 = 0.46), indicating that nearly half (46%) of the observed interannual variability of XCO_2 can be explained by interannual variations in local anthropogenic emissions in Hefei. This finding suggests that the accumulated anthropogenic emissions may drive increasing trends in atmospheric CO_2.

Against this backdrop, a further comparison between interannual increments in emission (ΔEmission) and in XCO_2 (ΔXCO_2) shows a positive correlation (r = 0.48, R^2 = 0.23), indicating a positive relationship in the fluctuations. However, it is not statistically significant (p = 0.14), which can be attributed to the small number of points (n = 11) or the dilution of this signal due to interannual variations in meteorological conditions and regional transport. Nevertheless, the positive association between the two time series and the positive trends in the increment series overall suggest the leading role of local anthropogenic emissions in the observed XCO_2 signals. Nevertheless, further investigation with longer time series and more sophisticated modeling approaches is warranted to better characterize interannual fluctuations.

The fastest growing source was that of the electricity and heat production sector, which increased from 5.1 kt in 2009 to 22.9 kt in 2020, representing an increase of 349% over the 12-year period. This sector accounted for

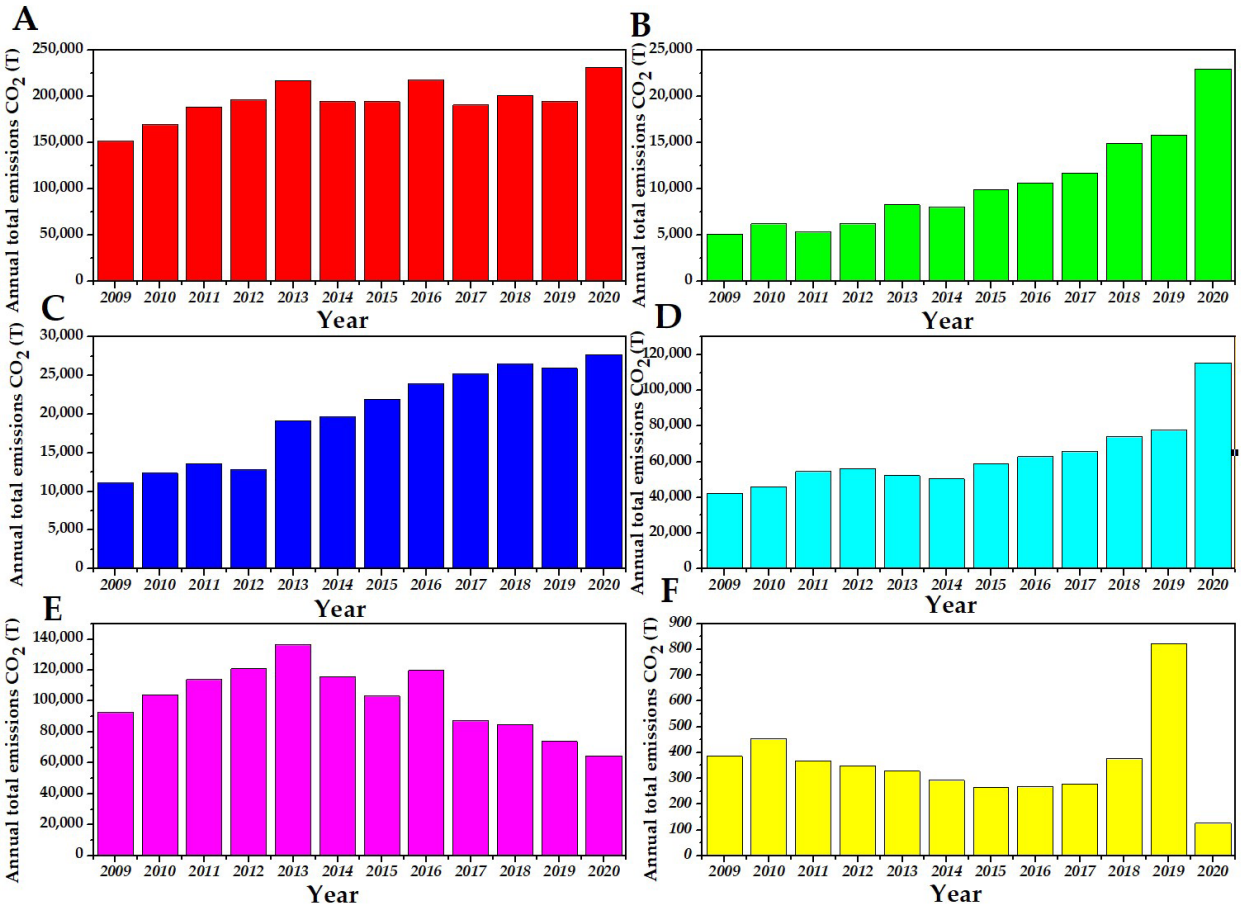

Figure 12. Carbon dioxide emissions by sector and year: (A) Total, (B) electricity and heat production, (C) residential and commercial, (D) industry and construction, (E) transport, and (F) international aviation.

23.5% of the total increase in emissions observed during the study period. However, throughout the observation period, industry and construction remained the largest emission source. Their emissions increased from 42.3 kt to 115.5 kt, demonstrating a 173% increase and accounting for 51.6% of the total increase. The increase in emissions thus reflected the overall rapid industrialization of Hefei.

The transport sector showed a different trend, with emissions rising to a peak of 92.6 kt in 2013 and thereafter declining to 64.6 kt in 2020. This may reflect the combined effect of rising vehicle ownership counterbalanced by progressive electrification of the fleet and improvements in fuel efficiency of conventional vehicles.

In summary, the power generation and industrial sectors collectively accounted for over 75% of the net increment in annual emissions, thus comprising the leading sources of anthropogenic CO_2 that drove the increase in XCO_2 in Hefei over the interannual period. These findings demonstrate that anthropogenic emissions dominate long-term trends, but their interannual variability is complex and requires trend analysis coupled with fluctuation analysis to provide a physical basis for controlling GHGs in fast-developing cities. In this regard, the monthly variation of anthropogenic CO_2 emissions for Hefei in 2020 is shown in Figure 13 to provide valuable insight into the dynamics of the emissions.

The results of the analysis of monthly anthropogenic CO_2 emissions for 2020 in Hefei are shown in Figure 13, demonstrating that anthropogenic CO_2 emissions in Hefei follow a strong seasonal cycle. Given the combination of seasonally varying patterns of emissions discussed above, together with backward-trajectory cluster analysis (Figure 11), the dominant mechanisms controlling the seasonal evolution of observed XCO_2 have been further elucidated, revealing marked seasonal regime shifts.

Generally, emissions peak in winter due to high demands for residential heating and cogeneration of heat and power. Backward trajectories mainly involve short-range, near-surface air transport during this season (Figure 11D), resulting in the accumulation of local emissions

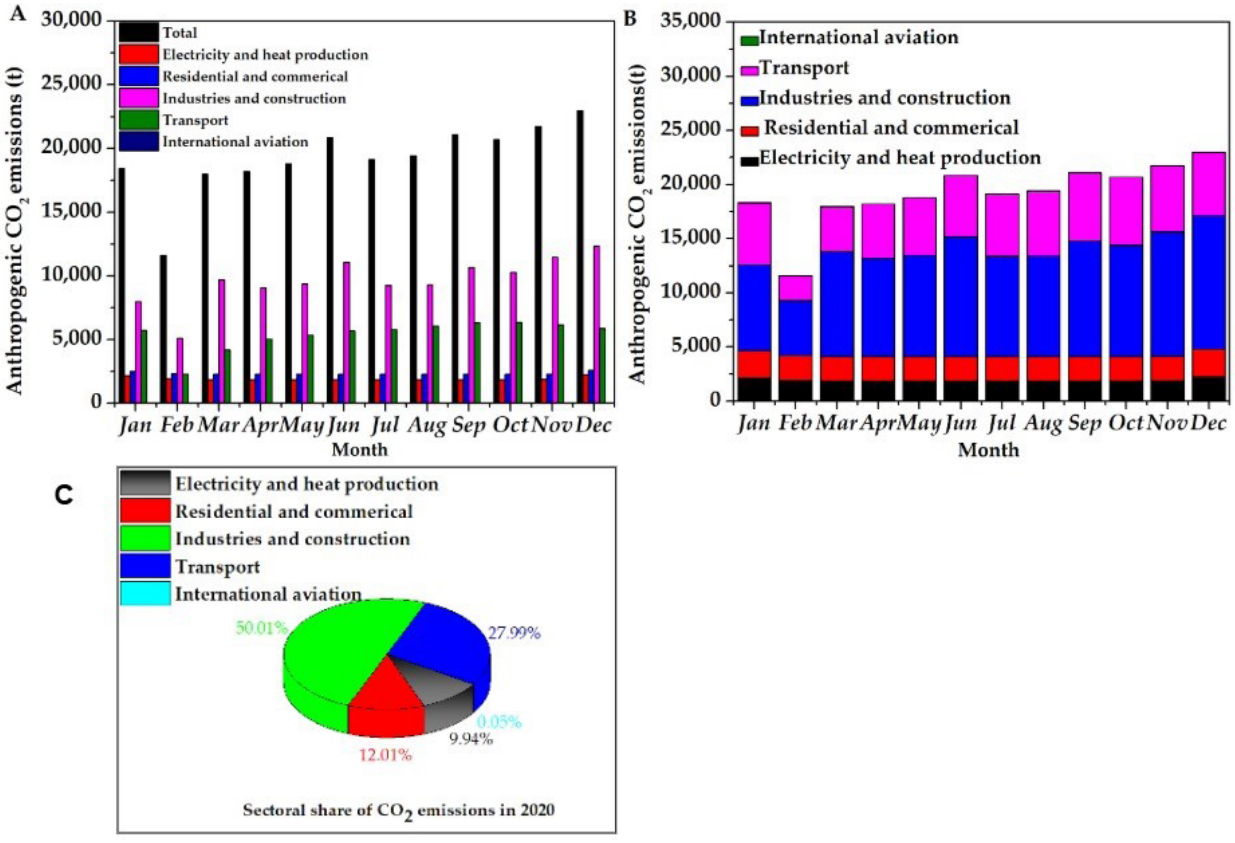

Figure 13. Anthropogenic CO_2 emission inventory for 2020. (A) Emissions by sector and total. (B) Stacked area plot of monthly sectoral emissions. (C) Annual sectoral emission shares.
Abbreviation: CO_2: Carbon dioxide.

under stable boundary-layer conditions. This underpins the relatively high absolute values of XCO_2 during winter and the relatively modest growth rates during that period.

In summer, although the power demand associated with cooling leads to increased emissions in the power sector, other sectoral emissions, particularly from industries, are low. More importantly, summer is characterized by a dominant influence of marine air mass inflow (Figure 11B). Such transport leads to substantial dilution of local signals. In addition, this period corresponds to peak photosynthetic activity and thus the strongest terrestrial biosphere CO_2 sink. Emission increments are offset by dilution and enhanced biological uptake, leading to the lowest XCO_2 growth rate of the year.

The influence of seasonality on background levels and episodic injections at the regional scale is most pronounced in autumn. In this season, industry- and power-sector emissions remain high. However, a significant number of air masses trace back to the heavily agricultural northeastern areas, which coincides with the peak period of regional straw burning (Figure 11C). The superposition of strong local industrial emissions and biomass-burning plumes from upwind regions explains the highest seasonally averaged XCO_2 growth rates during autumn.

During spring, emissions increase gradually after a slowing of industrial activities over winter, and long-range transported emissions from industrialized northern China also intermittently influence the region (Figure 11A). However, following vegetation greening, the terrestrial biosphere again acts as a carbon sink that mitigates this positive emission signal, thus producing relatively moderate XCO_2 growth rates during spring. Hence, spring is a transitional period showing a mixture of emission- and biologically driven processes.

A decoupling between the local emission baseline and the long-term variation in the observed XCO_2 seasonal cycle could thus be demonstrated at the city scale of Hefei through coupling the emission inventory with satellite retrievals and trajectory–cluster analyses. Specifically, on interannual timescales, long-term sustained growth in both industry and electricity sectors constituted >75% of total increment emissions and therefore determined the dominant driver behind the long-term increasing trend. Seasonally, the varying roles of local emission-structure changes (e.g., strong heating demand in winter and cooling-related power demand in summer) with regional external transport events (e.g., biomass burning in autumn) and seasonally varying importance of biogenic processes (e.g., photosynthetic uptake in summer) jointly or competitively determine the seasonality of XCO_2 evolution.

To explicitly position these findings within the broader scientific record, this study contributes to the understanding of urban GHG dynamics in three specific aspects. First, it enriches the observational database for rapidly industrializing urban hotspots—areas that exert a disproportionate impact on global GHG budgets but often lack integrated constraints. By bridging more than a decade of satellite retrievals (2009–2020) with high-resolution ground-based measurements, this work provides a comprehensive empirical case study for the Yangtze River Delta region. Second, the research refines the application of co-emission analyses by quantitatively demonstrating the seasonal decoupling of XCO_2 and XCH_4. Rather than treating anthropogenic correlations as static, the findings systematically document how summer biogenic fluxes and specific air mass transport processes dilute shared fossil fuel combustion signatures. Finally, by explicitly linking atmospheric variability to specific drivers, such as the 75% emission contribution from the industrial and power sectors, and the modulation by autumn biomass burning plumes, this study integrates observational data with emission inventories, thereby offering a verified scientific basis for formulating seasonally adaptive mitigation strategies in similar super-regional development hubs.

4. Conclusion

This study integrated satellite observations, ground-based measurements, atmospheric transport modeling, and emission inventories to elucidate the spatiotemporal dynamics and driving forces of atmospheric XCO_2 and XCH_4 in Hefei, a rapidly industrializing city.

Both XCO_2 and XCH_4 exhibit long-term growth rates exceeding their respective global averages. This rapid accumulation, demonstrated by significant interannual anomalies (e.g., coal-related emissions and El Niño-driven wetland enhancements), quantitatively highlights the disproportionate impact of rapidly developing urban-industrial regions as critical global GHG hotspots.

Strong co-variations between XCO_2 and XCH_4 in winter, spring, and autumn indicate predominantly shared anthropogenic sources from fossil fuel combustion. However, this correlation significantly weakens in summer. This seasonal decoupling is primarily driven by the superposition of active biogenic processes (enhanced photosynthetic CO_2 uptake versus increased CH_4 emissions from wetlands/paddy fields) and the transport of clean marine air masses.

Local GHG concentrations are heavily modulated by seasonal atmospheric transport patterns. For instance, the maximum seasonal growth of XCO_2 observed in autumn is exacerbated by the long-range transport of regional

biomass burning plumes. Conversely, summer XCH_4 maxima are sustained by continuous local agricultural emissions coupled with favorable medium-range transport conditions.

From a climate policy and emissions management perspective, the source–sink–transport integrated analysis demonstrates that achieving carbon neutrality in similar rapidly industrializing cities requires highly targeted strategies. First, since the industrial, construction, and energy supply sectors account for approximately 75% of the regional GHG increments, deep decarbonization within these specific sectors remains the top priority. Second, mitigation policies must be seasonally adaptive. For example, stringent cross-regional control of agricultural straw burning is crucial in autumn to mitigate XCO_2 peaks, while optimizing water and fertilizer management in local paddy fields is necessary to curb summer XCH_4 emissions.

Despite these insights, several limitations of this study should be acknowledged. The ground-based validations predominantly rely on a limited number of observation sites, which may constrain the capture of fine-scale spatial heterogeneity across the entire urban area. Additionally, inherent uncertainties exist in both satellite retrievals and bottom-up emission inventories. To address these limitations, future research should focus on establishing a denser, multi-node ground-based observation network within the city. Furthermore, integrating isotopic measurements and high-resolution atmospheric inversion models will be essential to further reduce uncertainties and achieve more precise source apportionment of urban GHGs.

Acknowledgments

The processing environment of the PROFFIT program was provided by the Institute of Meteorology and Climate Research. We thank Qiansi Tu and Frank Hase for their support in the inversion analysis.

Funding

This research was supported by the High-Level Talents Project of Wanxi University (WGKQ2021007) and the Academic Award for Top Talents in University Disciplines (2022) (gxyq2022063).

Conflict of interest

The authors declare that they have no known competing financial interests or personal relationships that could have appeared to influence the work reported in this paper.

Author contributions

*Conceptualizatio*n: Dandan Liu
Data curation: Dandan Liu
Formal analysis: Dandan Liu
Investigation: Dandan Liu
Methodology: Xiangyuan Liu, Dandan Liu
Software: Dandan Liu, Xiangyuan Liu
Supervision: Ke Tang, Ping Yu
Writing–original draft: Dandan Liu
Writing–review & editing: Dandan Liu

Availability of data

Data presented in this study are available on request from the corresponding author.

References

1. Forster PM, Smith CJ, Walsh T, *et al*. Indicators of Global Climate Change 2022: annual update of large-scale indicators of the state of the climate system and human influence. *Earth Syst Sci Data*. 2023;15(6):2295-2327.

   doi: 10.5194/essd-15-2295-2023

2. Barnes C, Boulanger Y, Keeping T, *et al*. Climate change more than doubled the likelihood of extreme fire weather conditions in Eastern Canada. 2023. Available from: https://ostrnrcan-dostrncan.canada.ca/handle/1845/270105 [Last accessed on].

3. Bellouin N, Davies W, Shine KP, *et al*. Radiative forcing of climate change from the Copernicus reanalysis of atmospheric composition. *Earth Syst Sci Data*. 2020;12(3):1649-1677.

   doi: 10.5194/essd-12-1649-2020

4. Saunois M, Martinez A, Poulter B, *et al*. Global methane budget 2000–2020. *Earth Syst Sci Data*. 2025;17(5):1873-1958.

   doi: 10.5194/essd-17-1873-2025

5. Keeling CD, Bacastow RB, Bainbridge AE, *et al*. Atmospheric carbon dioxide variations at Mauna Loa observatory, Hawaii. *Tellus*. 1976;28(6):538-551.

   doi: 10.1111/j.2153-3490.1976.tb00701.x

6. Dlugokencky EJ, Nisbet EG, Fisher R, *et al*. Global atmospheric methane: budget, changes and dangers. *Philos Trans R Soc A*. 2011;369(1943):2058-2072.

   doi: 10.1098/rsta.2010.0341

7. Jin C, Xue Y, Jiang X, *et al*. A long-term global XCO2 dataset: Ensemble of satellite products. *Atmos Res*. 2022;279:106385.

   doi: 10.1016/j.atmosres.2022.106385

8. Burton C, Lampe S, Kelley DI, *et al*. Global burned area increasingly explained by climate change. *Nat Clim Chang*. 2024;14(11):1186-1192.

   doi: 10.1038/s41558-024-02140-w

9. Alberti RCA, Lauvaux T, Vara-Vela AL, *et al*. Monitoring and modeling seasonally varying anthropogenic and biogenic CO2 over a large tropical metropolitan area. *Atmos Chem Phys*. 2025;25(17):9803-9829.

doi: 10.5194/acp-25-9803-2025

10. Peters GP, Andrew RM, Canadell JG, *et al*. Key indicators to track current progress and future ambition of the Paris Agreement. *Nat Clim Chang*. 2017;7(2):118-122.

doi: 10.1038/nclimate3202

11. Basu S, Lan X, Dlugokencky E, *et al*. Estimating emissions of methane consistent with atmospheric measurements of methane and δ13C of methane. *Atmos Chem Phys*. 2022;22(23):15351-15377.

doi: 10.5194/acp-22-15351-2022

12. Hu Y, Yue X, Tian C, *et al*. Identifying the main drivers of the spatiotemporal variations in wetland methane emissions during 2001–2020. *Front Environ Sci*. 2023;11:1275742.

doi: 10.3389/fenvs.2023.1275742

13. Crippa M, Guizzardi D, Pagani F, *et al*. GHG emissions of all world countries. Publications Office of the European Union; 2023.

doi: 10.2760/953332

14. Janardanan R, Maksyutov S, Wang F, *et al*. Country-level methane emissions and their sectoral trends during 2009–2020 estimated by high-resolution inversion of GOSAT and surface observations. *Environ Res Lett*. 2024;19(3):034007.

doi: 10.1088/1748-9326/ad2436

15. Hu H, Geng G, Xu R, *et al*. Notable uncertainties in near real-time CO2 emission estimates in China. *npj Clim Atmos Sci*. 2025;8(1):80.

doi: 10.1038/s41612-025-00991-4

16. Zheng B, Tong D, Li M, *et al*. Trends in China's anthropogenic emissions since 2010 as the consequence of clean air actions. *Atmos Chem Phys*. 2018;18(19):14095-14111.

doi: 10.5194/acp-18-14095-2018

17. Zhang L, Li T, Wu J, *et al*. Global estimates of gap-free and fine-scale CO2 concentrations during 2014–2020 from satellite and reanalysis data. *Environ Int*. 2023;178:108057.

doi: 10.1016/j.envint.2023.108057

18. Yokota T, Yoshida Y, Eguchi N, *et al*. Global concentrations of CO2 and CH4 retrieved from GOSAT: First preliminary results. *SOLA*. 2009;5:160-163.

doi: 10.2151/sola.2009-041

19. Kuze A, Suto H, Nakajima M, *et al*. Thermal and near infrared sensor for carbon observation Fourier-transform spectrometer on the Greenhouse Gases Observing Satellite for greenhouse gases monitoring. *Appl Opt*. 2009;48(35):6716-6733.

doi: 10.1364/ao.48.006716

20. Deng Z, Zhu B, Davis SJ, *et al*. Global carbon emissions and decarbonization in 2024. *Nat Rev Earth Environ*. 2025;6(4):231-233.

doi: 10.1038/s43017-025-00658-x

21. Zhang M, Liu G. Mapping contiguous XCO2 by machine learning and analyzing the spatio-temporal variation in China from 2003 to 2019. *Sci Total Environ*. 2023;858:159588.

doi: 10.1016/j.scitotenv.2022.159588

22. Buchwitz M, Reuter M, Schneising O, *et al*. The Greenhouse Gas Climate Change Initiative (GHG-CCI): Comparison and quality assessment of near-surface-sensitive satellite-derived CO2 and CH4 global data sets. *Remote Sens Environ*. 2015;162:344-362.

doi: 10.1016/j.rse.2013.04.024

23. Wunch D, Toon GC, Blavier JFL, *et al*. The total carbon column observing network. *Philos Trans R Soc A*. 2011;369(1943):2087-2112.

doi: 10.1098/rsta.2010.0240

24. Liu Z, Ciais P, Deng Z, *et al*. Carbon Monitor, a near-real-time daily dataset of global CO2 emission from fossil fuel and cement production. *Sci Data*. 2020;7(1):392.

doi: 10.1038/s41597-020-00708-7

25. Gisi M, Hase F, Dohe S, *et al*. XCO2-measurements with a tabletop FTS using solar absorption spectroscopy. *Atmos Meas Tech*. 2012;5(11):2969-2980.

doi: 10.5194/amt-5-2969-2012

26. Nisbet EG, Fisher RE, Lowry D, *et al*. Methane mitigation: methods to reduce emissions, on the path to the Paris agreement. *Rev Geophys*. 2020;58(1):e2019RG000675.

doi: 10.1029/2019rg000675

27. Tu Q, Hase F, Zhang Y, *et al*. Emission characteristics of greenhouse gases and air pollutants in a Qinghai-Tibetan Plateau city using a portable Fourier transform spectrometer and TROPOMI observations. *Atmos Chem Phys*. 2025;25(23):17779-17796.

doi: 10.5194/acp-25-17779-2025

28. Enting IG. Constraining atmospheric transport. In: *Inverse Problems in Atmospheric Constituent Transport*. Cambridge University Press; 2002:298-309.

doi: 10.1017/cbo9780511535741.019

29. Stein AF, Draxler RR, Rolph GD, *et al*. NOAA's HYSPLIT atmospheric transport and dispersion modeling system. *Bull Am Meteorol Soc*. 2015;96(12):2059-2077.

doi: 10.1175/bams-d-14-00110.1

30. Saunois M, Stavert AR, Poulter B, *et al*. The global methane budget 2000–2017. *Earth Syst Sci Data*. 2020;12(3):1561-1623.

doi: 10.5194/essd-12-1561-2020

31. Xu R, Tong D, Xiao Q, *et al*. MEIC-global-CO2: A new global CO2 emission inventory with highly-resolved source category and sub-country information. *Sci China Earth Sci*. 2023;67(2):450-465.

doi: 10.1007/s11430-023-1230-3

32. He Y, Chen R, Wu H, *et al*. Zhongguo nongye tan paifang kongjian geju ji yingxiang yinsu dongtai yanjiu [Spatial dynamics of agricultural carbon emissions in China and the related driving factors]. *Chin J Eco-Agric*. 2018;26(9):1269-1282. [In Chinese].

doi: 10.13930/j.cnki.cjea.171097